Temperature measurements in low-pressure, diamond-forming, premixed flames

Cite as: Journal of Applied Physics **84**, 4595 (1998); https://doi.org/10.1063/1.368685
Submitted: 27 February 1998 . Accepted: 07 July 1998 . Published Online: 27 October 1998

J. S. Kim, and M. A. Cappelli

Temperature measurements in low-pressure, diamond-forming, premixed flames

J. S. Kim and M. A. Cappelli[a)]
Thermosciences Division, Department of Mechanical Engineering, Stanford University, Stanford, California 94305-3032

(Received 27 February 1998; accepted for publication 7 July 1998)

Measurements of temperature in low-pressure, diamond-forming, premixed flames are described. Optical emission spectroscopy was used to determine the rotational temperature of CH radicals in the flame by analyzing the spectra of the *R*-branch of the $A\ ^2\Delta \rightarrow X\ ^2\Pi(0,0)$ CH electronic transition near 430 nm. Emission spectroscopic measurements were taken in stagnation-point flames of three different fuel types; CH_4–O_2, C_2H_4–O_2, and C_2H_2–O_2 flames, all of which have been previously used in the synthesis of diamond films. The emission-based rotational temperatures are found to be in good agreement with temperature measurements from thermocouples for the CH_4–O_2 flame, when a correction is made to the thermocouple measurements for radiation losses. The measurements show that peak flame temperatures are higher than the adiabatic flame temperatures for both C_2H_4–O_2, and C_2H_2–O_2 flames; a result that is also predicted by a numerical simulation of the stagnation-point strained flame that accounts for detailed finite-rate gas-phase chemistry and heterogeneous surface reactions. © *1998 American Institute of Physics.* [S0021-8979(98)06619-5]

I. INTRODUCTION

Hirose and Mitsuizumi[1] were the first to demonstrate that polycrystalline diamond films can be synthesized on temperature-controlled surfaces immersed in the ''feather'' of an atmospheric pressure flame generated by a conventional C_2H_2–O_2 premixed brazing torch. In that study, high-quality diamond films were deposited over an area of about 10 mm^2 at rates of 100–150 μm/h. This deposition rate was at least 10–100 times greater than that of low-pressure plasma and hot-filament chemical vapor deposition (CVD) methods, which, at that time, were the most common methods used to deposit diamond films. While this atmospheric pressure C_2H_2–O_2 flame process drew considerable attention and was shortly afterwards reproduced in other laboratories,[2–4] extending its capabilities to deposit over larger areas became a formidable challenge. Methods of scanning the flame[5] or using multiple flames[6] led to some progress in increased deposition area, but a notable improvement was made by using highly strained, atmospheric pressure C_2H_2–O_2–H_2 flat flames in which the flame zone occupies an extended area larger than that of the nozzle, and the flame is stabilized very near the substrate surface.[7] The use of these highly strained flames resulted in a tenfold increase in deposition area, however, concomitant with this approach was a need to develop improved methods of accommodating the extremely high heat fluxes, typically, in the range of 0.5–1 kW/cm^2.[8]

Low-pressure C_2H_2–O_2 flat flames were shown to overcome some of the difficulties associated with the use of atmospheric flame deposition methods.[9–11] The trade-off, however, is that low-pressure flame methods result in deposition rates that are generally less than those obtained at atmospheric pressure, despite the potentially significant increase in deposition area [as large as ~20 cm^2 (Ref. 12)]. In some specialized applications where very thin diamond films are required, such as in thin-film coatings on cutting tool inserts, the relative ease of control of substrate temperature and increased deposition area may be more of a factor than the deposition rate when determining the overall process costs. Still, in comparison to other diamond CVD methods, the relatively high cost of acetylene makes either low-pressure or atmospheric pressure flame synthesis methods less competitive than other diamond CVD techniques in most applications.[13,14] This has stimulated research in the development of the use of less expensive fuels such as ethylene and methane.[15,16] The demonstration of diamond film growth from low pressure methane/oxygen flames is especially promising since methane is the largest component in natural gas and is by far the cheapest of the simple hydrocarbon fuels.

In either low-pressure or atmospheric pressure flames, an important flow property that directly affects the deposition of diamond is the flame temperature. Higher flame temperatures produce higher concentrations of atomic hydrogen, which is known to be directly involved in the diamond growth kinetics. In developing models that describe the flame synthesis process, the prediction of the concentration of H and other potentially important gas-phase species such as CH_3, C_2H_2, O, and O_2, will require accurate predictions of the flame temperature.

In this study, we present a comparison of the measured and predicted temperature profiles in CH_4–O_2, C_2H_4–O_2, and C_2H_2–O_2 flames. Temperatures are measured using two approaches: an immersed thermocouple probe (where possible) and optical emission spectroscopy. Optical emission spectroscopy is performed to determine the rotational tem-

a)Author to whom correspondence should be addressed. Electronic mail: cap@leland.stanford.edu.

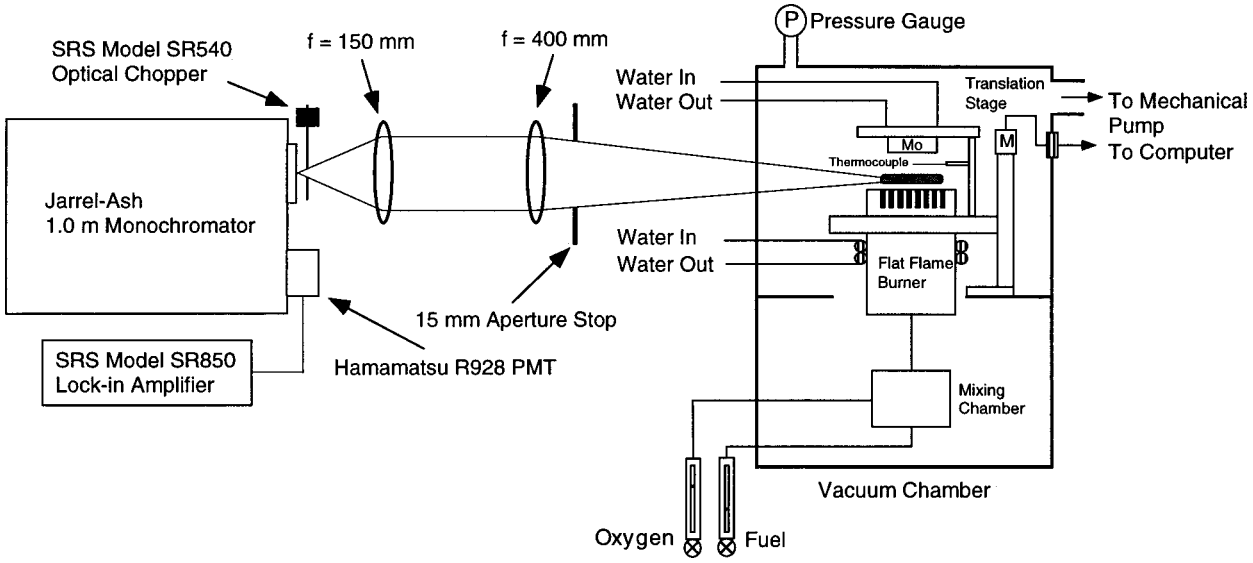

FIG. 1. Schematic of the experimental setup for flame temperature measurements.

perature of CH in the flame by analyzing the relative intensities of the rotational lines within the $A\ ^2\Delta \rightarrow X\ ^2\Pi(0,0)$ (pure rotational) electronic transition of CH. Comparisons of the measured and predicted flame temperatures are made using a numerical model that we have developed previously.[17] These studies allow us to directly assess the model's capability to predict the flame temperature in these flames, which have very strong velocity gradients (highly ''strained'' flames).

II. EXPERIMENT

The low-pressure flame apparatus employed in this study is described in detail elsewhere.[11] A schematic of the burner and vacuum chamber is shown in Fig. 1. The burner consists of a water-cooled cylindrical brass mixing chamber capped off at the top with a brass disk which has an array of 131 uniformly spaced 1 mm diam holes through which the premixed reactants flow. The diameter of the array of holes is 2.6 cm. For the measurements taken here, the burner and substrate were mounted on a stepper motor-driven translation stage that was computer controlled. A molybdenum rod, 3.2 cm in diameter, served as a substrate. The substrate temperature was monitored by inserting a *K*-type thermocouple probe into the molybdenum rod from the backside through a 1 mm diam channel, resting approximately 1 mm from the substrate surface.

A. Thermocouple measurements

The gas-phase temperature in low-pressure methane–oxygen flames was measured using thermocouple probes immersed directly into the flame region. Care is needed in using thermocouples for such measurements, since the thermocouple junction temperature that is established is a complex balance between energy transfer by conduction along the thermocouple wires, convection from the flame, and catalytic radical recombination on the thermocouple bead surface. Radiation and convection effects can be accounted for if the emissivities and convective heat transfer coefficients are known or can be estimated. Conduction effects can also be minimized by careful selection of the wire cross-sectional area in comparison to the area of the thermocouple bead,[18] and are negligible in the studies reported on here. Energy transfer through catalytic surface recombination heating occurs because platinum and/or other transition metals often used for high-temperature environments tend to have very high surface recombination coefficients for radicals such as atomic hydrogen and atomic oxygen. In addition, common thermocouple alloys often react with hydrocarbon radicals causing the thermocouple to become brittle and a change in its response. It is common practice then to protect the thermocouple junction from the reactive chemical environment with a ceramic coating that can also serve as a barrier to radical recombination. Previous measurements of flame temperatures have shown that coatings of ceramic adhesives can reduce or eliminate this catalytic recombination heating,[19,20] while protecting the junction and adding only a small thermal resistance to conduction.

The thermocouples used in this study were of the *B*-type (Pt–30% Rh/Pt–6% Rh), with 250 μm diam lead wires and a 0.55 mm diam junction bead. The bead was coated with a commercially available high-temperature ceramic adhesive (Aremco, Ceramabond 571). The thermocouple bead and connecting wires were cleaned with distilled water and methanol prior to being coated and fired, in accordance with the accompanying specifications from the ceramics manufacturer. The coated thermocouples (lead wires and bead) had more of a cylindrical shape with a nominal diameter of 0.9 mm.

The measured temperatures were corrected for radiation effects by treating the radiation exchange between the thermocouple, burner surface, substrate surface, and remaining enclosure area as a four-body problem (four nodes; $N=1-4$) using a circuit equivalent analysis.[21] For this analysis, we must assume that the surfaces behave as gray bodies of known emissivities. Energy, transferred to the thermocouple ($N=1$) by convection from the flame, is radiated to

TABLE I. Equations for view factors. Body 1: thermocouple, body 2: burner surface, body 3: substrate, and Body 4: chamber. (A_1, A_2, A_3, and A_4: Areas of thermocouple, burner surface, substrate, and chamber. $\xi_1 = 1/2[1-1/(1+R^2)^{1/2}]$, $R=r_{\text{burner}}/d_1$, where r_{burner} is the radius of the burner and d_1 is the distance between the thermocouple and burner surface. $\xi_2=1/2[1-1/(1+R^2)^{1/2}]$, $R=r_{\text{substrate}}/d_2$, where $r_{\text{substrate}}$ is the radius of the substrate and d_2 is the distance between the thermocouple and substrate. $\xi_3=1/2[X-(X^2-4(R_2/R_1)^2)^{1/2}]$, $R_1=r_{\text{burner}}/d_3$, $R_2=r_{\text{substrate}}/d_3$, $X=1+(1+R_2^2)/R_1^2$, where d_3 is the distance between the substrate and burner surface.

View factor, F_{ij}	View factor, F_{ij}
$F_{11}=0$	$F_{31}=(A_1/A_3)F_{13}$
$F_{12}=\xi_1$	$F_{32}=(A_2/A_3)F_{23}$
$F_{13}=\xi_2$	$F_{33}=0$
$F_{14}=1-F_{12}-F_{13}$	$F_{34}=1-F_{31}-F_{32}$
$F_{21}=(A_1/A_2)F_{12}$	$F_{41}=(A_1/A_4)F_{14}$
$F_{22}=0$	$F_{42}=(A_2/A_4)F_{24}$
$F_{23}=\xi_3$	$F_{43}=(A_3/A_4)F_{34}$
$F_{24}=1-F_{21}-F_{23}$	$F_{44}=1-F_{41}-F_{42}-F_{43}$

the surrounding three surfaces ($N=2-4$) in accordance with:

$$hA_1(T_f-T_1)=\sum_{N=2}^{4}\frac{J_1-J_N}{1/A_1F_{1N}}. \tag{1}$$

Here, h is the convective heat transfer coefficient, T_f is the local flame temperature, T_1 is the thermocouple temperature, A_1 is the thermocouple surface area, F_{ij} is the radiation view factor (see Table I for the values used) for radiation exchange between surfaces i and j, and J_i is the radiosity of ith surface. To estimate $h=\kappa Nu/D$ we assume the empirical relation between the Nusselt number (Nu) and Reynolds number (Re) given by Kaskan:[22]

$$\text{Nu}=0.8(\text{Re})^{0.25}. \tag{2}$$

Here, D is the coated thermocouple diameter and κ is the flame thermal conductivity. The Nu and Re are determined from the transport properties of the flame, predicted using our flame code described previously,[17] averaged over the burner-to-substrate distance. Typical values of the thermal conductivity and kinematic viscosity (needed for Re) used in this estimate are $\kappa=0.28$ W/m K and $\nu=1.36\times10^{-4}$ m^2/s, respectively.

An energy balance on the four surfaces exchanging radiation gives[21]

$$\frac{\sigma T_i^4-J_i}{(1-\epsilon_i)/\epsilon_i A_i}=\sum_{j\neq i}\frac{J_i-J_j}{1/A_iF_{ij}}. \tag{3}$$

Here, ϵ_i are the gray-body emissivities, taken from Siegel and Howell,[23] and are listed in Table II.

Together, Eqs. (1) and (3) constitute five equations in five unknowns (J_1-J_4, and T_f), which can be solved iteratively, as the surface temperatures (T_1-T_4) are determined experimentally.

B. Optical emission measurements

Spectroscopic emission measurements were performed to determine the rotational temperature of CH in the flame from the relative intensity of the rotational lines associated with the $A\ ^2\Delta\rightarrow X\ ^2\Pi(0,0)$ (pure rotational) electronic transition. This chemiluminescence, centered near 430 nm, from the excited CH ($A\ ^2\Delta$) molecules is a major source of visible light from hydrocarbon flames. Gaydon and Wolfhard[24] have previously shown that the rotational energy distribution of CH molecules in this electronic state is well described by a Boltzmann distribution and that the corresponding temperature is equilibrated with the flame translational temperature. This is not the case for the vibrational temperature, which, in low-pressure flames, can be far removed from equilibrium.

TABLE II. Values of emissivities.

	Emissivity, ϵ
Substrate, molybdenum	0.10–0.18
Burner, brass	0.60–0.80
Thermocouple, magnesia	0.16–0.20
Vacuum chamber, stainless steel	0.74–0.87

The intensity (I) of a spectral emission line within a rotational manifold originating from an upper state having a total angular momentum quantum number (rotational quantum number: N', plus the electron-spin quantum number: $\pm1/2$), $J'=N'\pm1/2$, and terminating on a lower state having a quantum number, $J''=N''\pm1/2$, is given by

$$I=CS_{J'J''}\lambda^{-4}\exp(-E_{J'}/kT). \tag{4}$$

Here, λ is the transition wavelength; T is the rotational temperature (which is assumed to be equilibrated with the flame temperature, T_f); k is Boltzmann's constant; C is a proportionality constant, which is the same for all rotational transitions within the manifold; $E_{J'}$ is the energy of the upper rotational state of the transition; and $S_{J'J''}$ is the Hönl–London factor, which accounts for the relative branching strength of rotational transitions within the manifold.

These measurements concentrated on the analysis of the relative strength of the R-branch transitions ($\Delta J=J'-J''=+1$), which are widely separated, and for which transitions terminating on rotational states with $J''=N''+1/2$, i.e., the $R_1(N'')$ transitions, and $J''=N''-1/2$, i.e., $R_2(N'')$ transitions, are easily resolved. The transition wavelengths, Hönl–London factors, and upper state energies, $E_{J'}$ for these R-branch transitions are given in Table III.

From Eq. (4), we would expect that a ''Boltzmann plot'' of the natural logarithm of the experimentally measured weighted intensities

$$\ln(I\lambda^4/S_{J'J''})=-(E_{J'}/kT)+\ln C, \tag{5}$$

versus $E_{J'}/k$ should return a straight line, and the slope of this line should be the inverse of the temperature. In practice, the intercept includes, in addition to the constants of proportionality given in Eq. (4), constants related to the absolute response of the instrumentation used to isolate the spectral features and record intensity.

Spectroscopic measurements were conducted across a line-of-sight passing through the centerline of the flames between the burner surface and substrate at several axial loca-

TABLE III. Wavelength, Hönl–London factors, and rotational term energies for the *R*-branch transitions of from the $A\ ^2\Delta \rightarrow X\ ^2\Pi(0,0)$ band of CH.

	Values for $R_1(N'')$ transitions			Values for $R_2(N'')$ transitions		
N''	λ (nm/air)	$S_{J'J''}$	E'_{rot} (cm^{-1})	λ (nm/air)	$S_{J'J''}$	E'_{rot} (cm^{-1})
11	424.460	7.825	1831.90	424.246	7.234	1831.00
12	423.725	8.319	2162.10	423.612	7.736	2161.34
13	423.104	8.815	2518.10	422.977	8.238	2517.39
14	422.486	9.311	2899.40	422.349	8.739	2898.75
15	421.873	9.807	3305.50	421.721	9.240	3304.91
16	421.261	10.300	3735.91	421.097	9.741	3735.43
17	420.658	10.800	4190.10	420.475	10.240	4189.66
18	420.060	11.300	4667.70	419.864	10.740	4667.28
19	419.473	11.800	5167.90	419.256	11.240	5167.50
20	418.897	12.290	5690.70	418.662	11.740	5690.00

tions. Emission measurements were taken from all three flames of different fuel types (CH_4–O_2, C_2H_4–O_2, and C_2H_2–O_2) at selected values of the flame equivalence ratio ϕ, operating pressure P, cold gas velocity u, and distance between the burner surface and the substrate d. The experimental conditions are listed in Table IV. With the exception of the methane flame, the experimental conditions for temperature measurements were the same as those used for depositing diamond. A slightly leaner flame was operated for CH_4–O_2 mixtures mainly due to the observation that the methane flame could not be stabilized at diamond growth conditions with the presence of the thermocouple within the flame zone.

The experimental spectroscopic setup for the flame temperature measurements is shown in Fig. 1. The flame is viewed through a side window at right angles to the axis and its emission is imaged onto the entrance slit of a Jarrel–Ash (1.0 m focal length) monochromator by a collimating (40 mm focal length) and a focusing (150 mm focal length) lens. A 15 mm aperture stop was placed in front of the first collection lens to stop down the collection volume, thereby increasing the depth of focus. The aperture stop gives a collection $f/\#$ of 27 and a depth of focus of 0.8 mm. This optical configuration gave rise to an image magnification of 0.375, and, with the entrance and exit slit widths set at 50 μm, and slit heights of 100 μm, the system spectral resolution was found to be 0.03 nm. The acceptance cone for the emission using this optical collection configuration gave rise to an estimated axial resolution of approximately 0.3 mm. The signal at the exit slit was acquired with a photomultiplier tube and phase-sensitive detection was used to discriminate against stray background light.

TABLE IV. Experimental conditions for emission measurements.

	C_2H_2–O_2 flame	C_2H_4–O_2 flame	CH_4–O_2 flame
ϕ	2.31	2.35	1.58
P, Torr	42	50	100
u, cm/s	390	195	73
d, cm	0.74	0.74	0.74

III. SIMULATIONS

The numerical model of the flame synthesis process developed in our laboratory is described in detail elsewhere.[17] The model consists of a quasi-two-dimensional representation of the flame in a stagnation-flow geometry. It treats the burner as an infinite diameter disk through which a uniform flow of premixed gases emerges at a specified (cold gas) velocity and temperature (measured with a thermocouple in the burner housing). The substrate, also treated as an infinite diameter disk at a specified temperature, is located a finite distance downstream of the burner. Numerical integration of the governing equations for overall mass, momentum, energy, and individual species conservation allows the prediction of the velocity (axial and radial), temperature, and species mole fraction profiles between the burner surface and the substrate. The governing equations are discretized using a finite central difference approximation, and the resulting system of algebraic equations is solved iteratively using a hybrid Newton/time-integration boundary-value-problem solver.[25]

The numerical model interfaces to a range of subroutines which are used to treat finite-rate gas-phase and heterogeneous surface reactions. The CHEMKIN II subroutine library[26,27] is used to compute the overall net reaction rates and thermodynamic properties of the flame constituents. The multicomponent transport properties are evaluated using the subroutine package called TRANSPORT.[28] The SURFACE CHEMKIN subroutine package[29] is used to compute the overall net reaction rates for active surface sites, thereby coupling surface sites to gas-phase radical fluxes to the surface.

The gas-phase reaction mechanism employed is that of Miller and Melius.[30] It includes a total of 50 species and 218 elementary reactions, originally developed for simulating fuel-rich, near-sooting hydrocarbon flames. A methyl-based heterogeneous mechanism proposed by Harris[31] is used to describe the growth of diamond. This mechanism prescribes H, H_2, and CH_3 as active gas-phase species which participate through a sequence of 12 elementary reactions to lead to the formation of bulk sp^3 hybridized carbon (diamond).

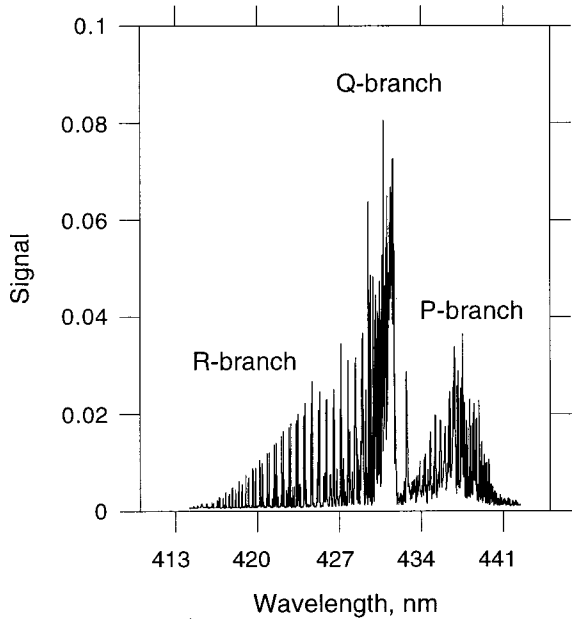

FIG. 2. A resolved scan of the three rotational branches of the $A\ ^2\Delta \rightarrow X\ ^2\Pi(0,0)$ band of CH for a C_2H_2–O_2 flame at $P=42$ Torr.

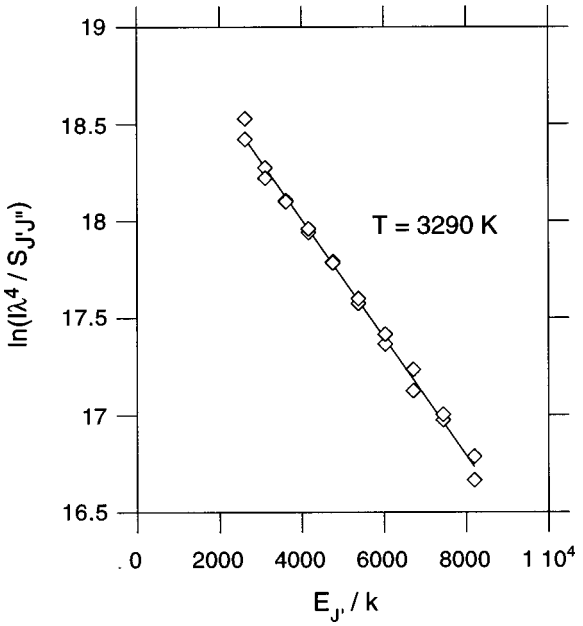

FIG. 4. Boltzmann plot for Fig. 3.

IV. RESULTS AND DISCUSSION

Figure 2 shows a typical survey scan of the three rotational branches constituting the $A\ ^2\Delta \rightarrow X\ ^2\Pi(0,0)$ band of CH, obtained from the emission of a low-pressure C_2H_2–O_2 flame at 42 Torr. Among these three branches, the *R*-branch clearly has the most widely spaced lines, therefore, this set of lines is used to measure the flame temperature.

Figure 3 shows a resolved scan of the *R*-branch with the lines assigned as $R(N'')$, where N'' is the rotational quantum number of the lower state to which the transition terminates. Note that these *R*-branch transitions are indeed doublets, with the longer wavelength transition in the doublet assigned to the $R_1(N'')$ transition. The corresponding Boltzmann plot of the transition intensities is shown in Fig. 4. The linearity of the plot indicates that the population of rotational energy states of the excited CH radicals follows a Boltzmann distribution. Because of the strong translational–rotational energy coupling, this distribution should be characterized by the flame temperature, derived from the slope of the line which best fits the data.

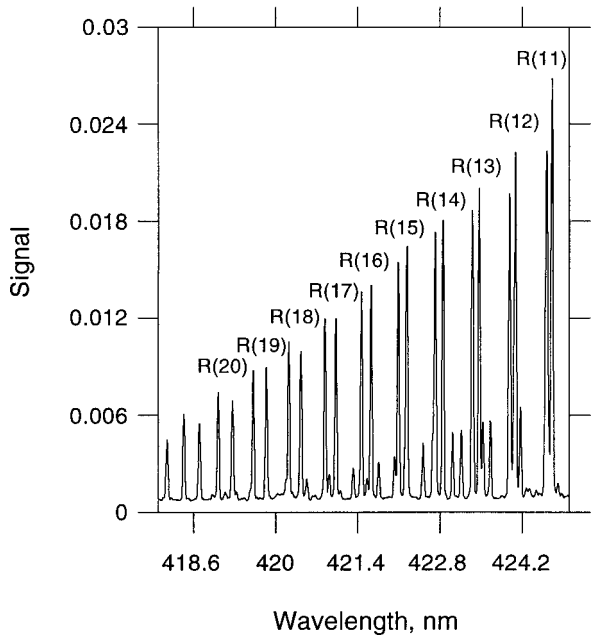

FIG. 3. A resolved scan of the *R*-branch for a C_2H_2–O_2 flame at $P=42$ Torr.

A low-pressure premixed CH_4–O_2 flame operating at $\phi=1.58$ and $P=100$ Torr was used as a test bed for comparing emission-based flame temperatures to those estimated from the immersed thermocouples. Figure 5 shows the measured uncorrected and radiation-corrected temperatures and their variation with distance from the substrate, which was held to a temperature of 1200 K. The results are given for an expected 0.16–0.20 range of emissivities for the coating material (magnesia). Varying the emissivities of the other three bodies (burner, substrate, and chamber) in the radiation-correction model had little effect on the temperature correction because of their relatively large surface area. The radiation corrections to the temperatures are significant, especially near the primary flame zone, where the corrections can be in excess of 500 K.

Comparisons are made between the spectroscopic and thermocouple-based temperature measurements in Fig. 6. Also shown in Fig. 6 are the results of the flame model predictions. The radiation-corrected profile shown here assumes emissivities of 0.10, 0.18, 0.80, and 0.75 for the emissivities of the substrate, thermocouples, burner, and chamber, respectively. These values were found to best reproduce the predicted shape of the temperature profile in the near-substrate region and are reasonable values for the materials employed. The radiation-corrected thermocouple temperatures are in very good agreement with the predicted temperatures, even in the flame zone very near the burner. The

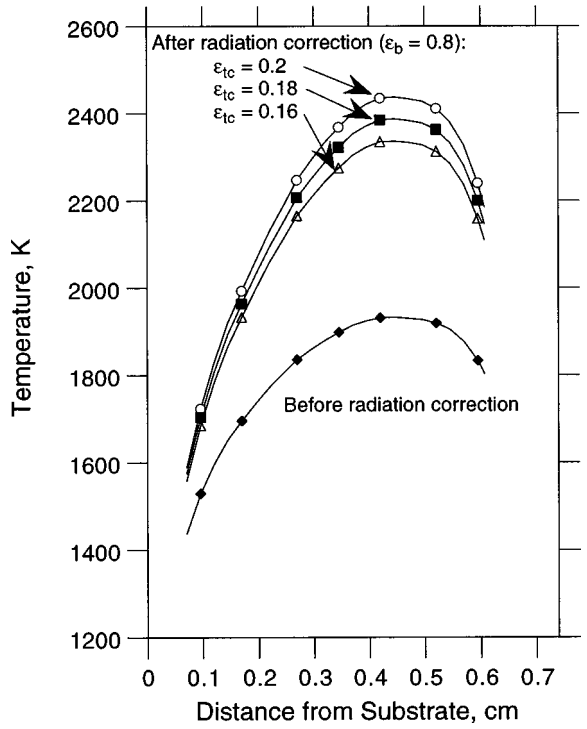

FIG. 5. Measured and radiation-corrected temperature profiles: CH_4–O_2 flames, $P=100$ Torr, $\phi=1.58$, and $T_s=850$ °C(±25 °C).

spectroscopic-based measurements, with no adjustable parameters, are also in good agreement with the predictions of the numerical model. The vertical error bars shown in Fig. 6 represent $\pm 2\sigma$ uncertainties in the linear fit to the Boltzmann plot. The growth of these error bars away from the flame zone arises from a decreasing signal-to-noise ratio caused by reduced signal levels, in part due to the lower CH concentrations in the cooler regions of the flame. For this methane flame, the peak flame temperature is predicted, and found

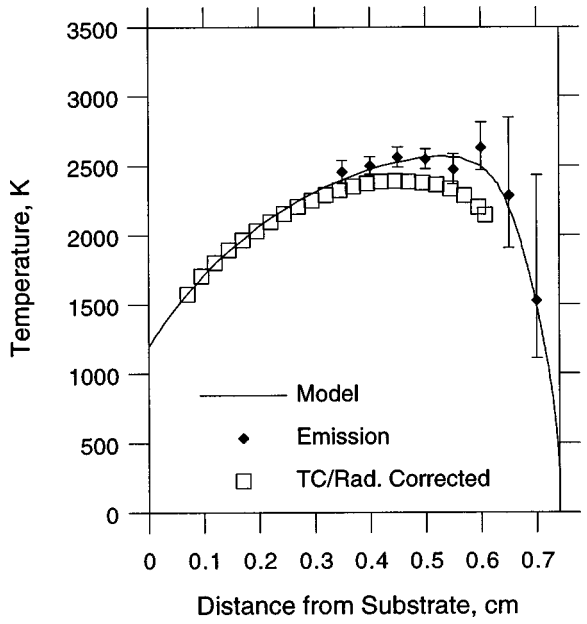

FIG. 6. Comparison of the predicted and measured temperatures: CH_4–O_2 flame.

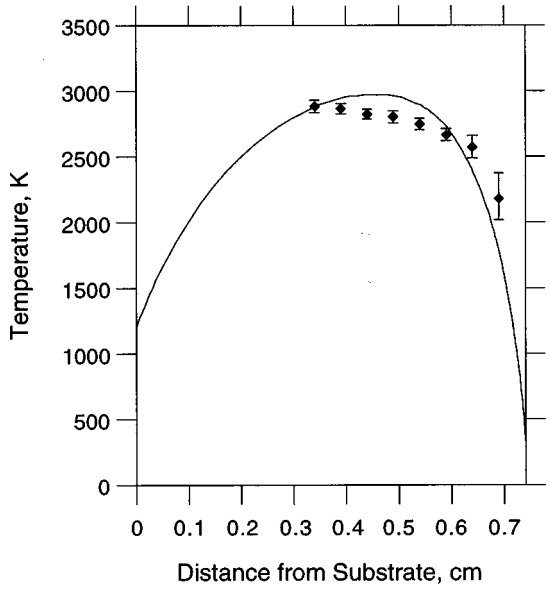

FIG. 7. Comparison of the predicted and measured temperatures: C_2H_4–O_2 flame.

experimentally, to be lower than the computed adiabatic flame temperature of 2734 K. The peak temperature determined by the spectroscopic measurement is 2630±170 K.

Because of the higher flame temperatures with ethylene and acetylene fuels, only spectroscopic measurements could be conducted to extract temperatures in flames of these types. Figure 7 shows a comparison of the temperature profile predicted by the model to those obtained spectroscopically for a C_2H_4–O_2 flame at $\phi=2.35$ and $P=50$ Torr. The measured and predicted flame temperatures are in good agreement. The predicted peak temperature is 2970 K, significantly higher than the adiabatic flame temperature (2592 K) at these flame operating conditions. The peak temperature obtained from the spectroscopic measurements is 2880±48 K, also significantly higher than the adiabatic flame temperature. While these superadiabatic temperatures are not uncommon for acetylene flames, to the best of our knowledge, these measurements appear to be the first reported temperature overshoots for ethylene flames. Superadiabatic temperatures have been predicted through simulations of atmospheric pressure C_2H_2–O_2–H_2 (Ref. 32) and low-pressure C_2H_2–O_2 flames.[33] They have also been previously measured by Bertagnolli and Lucht[34] in diamond-forming C_2H_2–O_2–H_2 flames at atmospheric pressure. This superadiabatic temperature in the C_2H_4–O_2 flame studied here arises because of the superequilibrium concentrations of unburned C_2H_2 in the postflame region. As shown in the graph of species mole fraction in Fig. 8, C_2H_2 maintains a superequilibrium mole fraction far downstream of the flame zone. A relatively long residence time is needed to oxidize unburned acetylene to its equilibrium level, conditions which are not present here because of the relatively high strain rates in these flames. Since the decomposition of acetylene and ethylene is endothermic at these flame temperatures, the loss of this energy sink leaves a greater supply of energy for molecular translation.

The predicted and measured temperatures for a C_2H_2–O_2 flame at $\phi=2.31$ and $P=42$ Torr are shown in Fig.

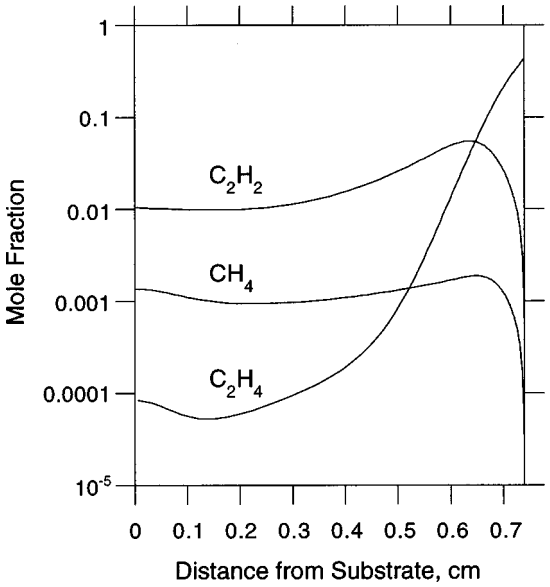

FIG. 8. Predicted spatial variation in mole fractions of three fuel species: C_2H_4–O_2 flame.

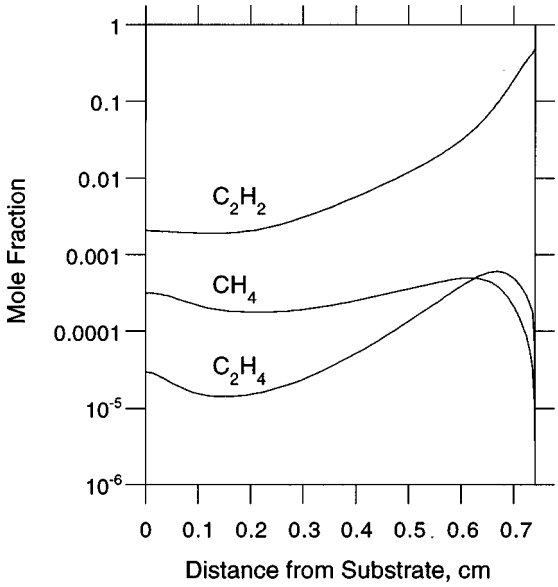

FIG. 10. Predicted spatial variation in mole fractions of three fuel species: C_2H_2–O_2 flame.

9. As expected, the peak flame temperature, predicted to be 3970 K at a distance of 2.2 mm above the burner surface, is significantly greater than the adiabatic flame temperature of 2965 K. While the maximum temperature derived from the spectroscopic measurements is somewhat lower than that predicted (3680 ± 80 K), it too exceeds the adiabatic flame temperature.

Figure 10 shows the predicted spatial variation in mole fractions of acetylene, ethylene, and methane. As in ethylene flames, C_2H_2 is found to maintain a superequilibrium concentration throughout the postflame region. The estimated fluid residence time for this C_2H_2–O_2 flame is approximately 1.9×10^{-3} s, which is about half of that for the C_2H_4–O_2 flame. It is, therefore, not surprising that the extent of the departure of this flame from its adiabatic flame temperature is greater than that of the C_2H_4–O_2 flame, as even less time is needed to oxidize unburned acetylene to its equilibrium concentration.

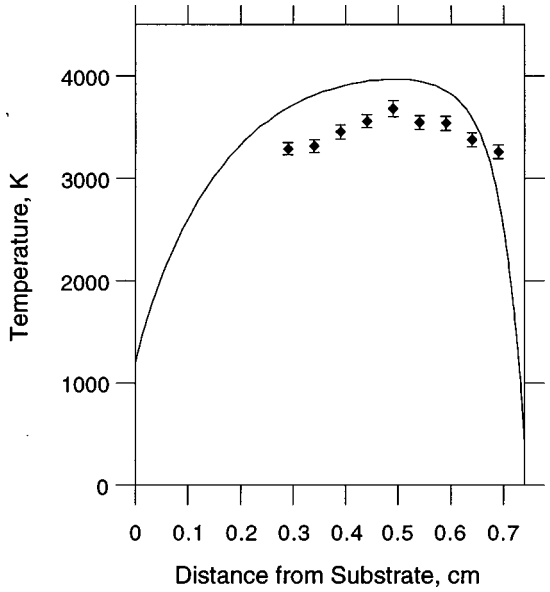

FIG. 9. Comparison of the predicted and measured temperatures: C_2H_2–O_2 flame.

The relatively good agreement between the predicted and measured temperatures for the three flame types studied adds confidence to the model's predictability of the flame structure. The model's ability to predict the temperature field is important in that many reactive radicals, some of which are critical to diamond growth chemistry, will be strongly coupled to the local temperature through a balance between temperature-sensitive controlling reactions. However, agreement between the predicted and measured temperature field, while encouraging, is not a sufficient condition for a model's ability to capture the radical concentration field, and so future experiments should focus on the measurements of species such as H and CH_3, which would provide a more critical test of the model's predictability.

V. SUMMARY

The results of spectroscopic and radiation-corrected thermocouple-based measurements of temperature in diamond forming CH_4–O_2, C_2H_4–O_2, and C_2H_2–O_2 flames are presented. The measured temperature profiles are in favorable agreement with numerical model predictions. In the case of the ethylene and acetylene flames studied here, the measured peak temperature is higher than the computed adiabatic flame temperature. Such superadiabatic temperatures have been predicted previously and have been observed experimentally in acetylene flames by other researchers. Temperatures in excess of the adiabatic flame temperatures are attributed to superequilibrium levels of unburned C_2H_2 present in the postflame region. The agreement between the predicted and measured temperatures adds confidence to the model's ability to predict the detailed flame structure, including the

radical concentration field. In addition, it further adds to the model's usefulness in determining optimum conditions for diamond synthesis.

ACKNOWLEDGMENTS

This research was supported in part by the Olin Aerospace Company and the National Science Foundation. The authors would like to acknowledge the assistance of P. V. Storm in collecting the emission spectra.

[1] Y. Hirose, in Proceedings of the 1st International Conference on the New Diamond Science and Technology (Japan New Diamond Forum, Tokyo, 1988), p. 38.
[2] L. M. Hanssen, W. A. Carrington, J. E. Butler, and K. A. Snail, Mater. Lett. **7**, 289 (1988).
[3] M. A. Cappelli and P. H. Paul, J. Appl. Phys. **67**, 2596 (1990).
[4] K. A. Snail and C. Craigie, Appl. Phys. Lett. **58**, 1875 (1991).
[5] Y. Tzeng, R. Phillips, C. C. Tin, Y. Chen, T. Srivinyunon, and C. Cutshaw, *in Diamond, Silicon Carbide and Related Wide Bandgap Semiconductors*, Boston, edited by J. T. Glass, R. Messier, and N. Fujimori (Materials Research Society, Pittsburgh, 1990), Vol. 162, p. 145.
[6] Y. Tzeng, R. Phillips, C. Cutshaw, T. Srivinyunon, B. H. Loo, and P. Wang, Appl. Phys. Lett. **58**, 2645 (1991).
[7] M. Murayama and K. Uchida, Combust. Flame **91**, 239 (1992).
[8] D. W. Hahn, C. F. Edwards, K. F. McCarty, and R. J. Kee, Appl. Phys. Lett. **68**, 2158 (1996).
[9] J. A. Cooper and W. A. Yarbrough, Proc. SPIE **1325**, 41 (1990).
[10] N. G. Glumac and D. G. Goodwin, Thin Solid Films **212**, 122 (1992).
[11] J. S. Kim and M. A. Cappelli, J. Mater. Res. **10**, 149 (1995).
[12] H. S. Shin, N. G. Glumac, and D. G. Goodwin, *in Proceedings of the 4th International Conference on New Diamond Science and Technology* (Materials Research Society, Pittsburgh, 1995), p. 27.
[13] K. V. Ravi, C. A. Koch, and D. Olson, in Proceedings of the 2nd International Conference Appl. Diamond Films and Related Materials, MYU, edited by M. Yoshikawa, M. Murakawa, Y. Tzeng, and W. A. Yarbrough, Tokyo, 1993, p. 491.
[14] J. V. Busch and J. P. Dismukes, Diamond Relat. Mater. **3**, 295 (1994).
[15] J. S. Kim and M. A. Cappelli, Appl. Phys. Lett. **65**, 2786 (1994).
[16] J. S. Kim and M. A. Cappelli, Appl. Phys. Lett. **67**, 1081 (1995).
[17] J. S. Kim and M. A. Cappelli, J. Appl. Phys. **72**, 5461 (1992).
[18] R. M. Fristrom, *Flame Structure and Processes* (Oxford University Press, New York, 1995).
[19] J. M. Madson and E. A. Theby, Combust. Sci. Technol. **36**, 205 (1984).
[20] K. A. Burton, H. D. Ladouceur, and J. W. Fleming, Combust. Sci. Technol. **81**, 141 (1992).
[21] J. P. Holman, *Heat Transfer*, 7th ed. (McGraw-Hill, New York, NY, 1990).
[22] W. E. Kaskan, 6th Symposium (International) on Combustion, The Combustion Institute, Pittsburgh, 1957, p. 34.
[23] R. Siegel and J. R. Howell, *Thermal Radiation Heat Transfer*, 3rd ed. (Hemisphere, Washington, DC, 1981).
[24] A. G. Gaydon and H. G. Wolfhard, Proc. Phys. Soc. London, Sect. A **199**, 89 (1949).
[25] J. F. Grvar, Technical Report No. SAND91-8230, Sandia National Laboratories, 1991.
[26] R. J. Kee, F. M. Rupley, and J. A. Miller, Technical Report No. SAND89-8009, Sandia National Laboratories, 1989.
[27] R. J. Kee, F. M. Rupley, and J. A. Miller, Technical Report No. SAND87-8215B, Sandia National Laboratories, 1987.
[28] R. J. Kee, G. Dixon-Lewis, J. Warnatz, M. E. Coltrin, and J. A. Miller, Technical Report No. SAND86-8246, Sandia National Laboratories, 1986.
[29] M. E. Coltrin, R. J. Kee, and F. M. Rupley, Technical Report No. SAND90-8003, Sandia National Laboratories, 1990.
[30] J. A. Miller and C. F. Melius, Combust. Flame **91**, 21 (1992).
[31] S. J. Harris, Appl. Phys. Lett. **56**, 2298 (1990).
[32] E. Meeks, R. J. Kee, D. S. Dandy, and M. E. Coltrin, Combust. Flame **92**, 144 (1993).
[33] N. G. Glumac, H. S. Shin, and D. G. Goodwin, Spring Western States Meeting, 21–22 March, UC Davis, The Combustion Institute, 1994.
[34] K. E. Bertagnolli and R. P. Lucht, 26th Symposium (International) on Combustion, The Combustion Institute, Pittsburgh, 1996, p. 1825.